

Multi-length scale modeling of chemical vapor deposition of titanium nitride coatings

M. GRUJICIC, S. G. LAI

Program in Materials Science and Engineering, Department of Mechanical Engineering,
241 Fluor Daniel Building, Clemson University, Clemson, SC 29634-0921, USA

E-mail: mica@ces.clemson.edu

Chemical Vapor Deposition (CVD) of TiN coatings has been analyzed at three different length scales: (a) At chemical reactor length scale, by solving the appropriate reactive-gas, fluid-dynamics, heat-transfer boundary value problem; (b) At the atomic scale, by applying a kinetic Monte Carlo method to model the deposition process in a stochastic manner and (c) At the coating-grain scale, by employing an improved van der Drift-type model to simulate the evolution of surface morphology, grain size distribution, evolution of the morphological and crystallographic texture, etc. in polycrystalline TiN coatings. It has shown that by combining the three modeling schemes, one can establish a direct link between the processes parameters and the microstructure (and thus the properties) of as CVD-grown TiN coatings. This, in turn, enables optimization of both the coating deposition process, and the microstructure and properties of CVD-grown coatings.

© 2001 Kluwer Academic Publishers

1. Introduction

Due to its high melting point, high hardness and excellent corrosion and erosion resistances, titanium nitride (TiN) is widely used as coating for machining and forming tools [e.g. 1]. TiN coatings are generally produced by either physical vapor deposition (PVD) [e.g. 2–5] or chemical vapor deposition (CVD) [e.g. 6–9] methods. CVD of TiN is generally carried out using either molecular nitrogen (N_2) gas or ammonia NH_3 gas as the source of nitrogen. In the present work, a multi-length scale analysis of the CVD of TiN coatings from $TiCl_4$ and NH_3 as the gaseous sources of titanium and nitrogen, respectively, is presented. It should be noted, however, that the approach used is fairly general and can be extended to both different Ti/N sources and to other types of coatings.

Processing of the TiN coatings by CVD from a precursor gas mixture containing $TiCl_4$ vapor, NH_3 gas and molecular hydrogen as the carrier gas at substrate temperatures in the range between 323 and 1900 K and the subambient pressures of 1–50 Torr (0.14–7.0 kPa) has become commercially viable over the last decade [e.g. 1, 10]. The gas mixture is typically heated using hot filaments, plasmas, combustion flames, and other means. While it is well-established that the chemical vapor deposition of TiN occurs as a result of chemical reactions between various $TiCl_4$ - and NH_3 -derived surface species, the mechanism of the TiN deposition is still not well understood. This is primarily caused by the fact that the atomic-scale events which lead to the deposition of TiN are difficult to study *in situ*. Hence, the current understanding of TiN deposition has been primarily gained through the use of computer modeling

and simulations and/or from the interpretation of *ex situ* experimental data.

In recent years a number of modeling approaches have been developed to analyze chemical vapor deposition of coatings and films. Some of the models [e.g. 11] deal with fluid dynamics and thermal energy effects of the reactive gas at the length scale of a CVD reactor. Such models enable computation of the average deposition rates but can not account for a number of important effects such as the effect of the local surface morphology and crystallographic orientation on the deposition process, incorporation of the lattice defects in the coating during deposition, etc. At the other length-scale extreme, there is a variety of the models which deal with atomic-scale events accompanying the CVD process. Among these models, some deal with the energetics of various surface configurations [12–18], while the others are used to determine the kinetic parameters of individual surface reactions [19–22]. In addition, molecular dynamics simulations are used to model the deposition process but such simulations are limited to only few milliseconds of the deposition time [e.g. 23]. Recently Battaile *et al.* [24] and Grujicic and Lai [25] demonstrated that a kinetic Monte Carlo method can be used to model CVD of single-crystalline films and coatings over tens of minutes of the deposition time. This approach is used in the present work to simulate the CVD process of TiN on the atomic scale. While atomic-scale simulations are useful in analyzing the deposition process of single-crystalline coatings and films, they are impractical for modeling the evolution of microstructure and texture in polycrystalline coatings and films. Recently, several models [26–28] have been proposed

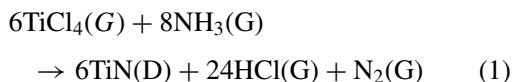
which can be used for simulation of the morphological and crystallographic texture and surface morphology in the thick polycrystalline coatings and films. Among these models developed by the present authors [27, 28], will be utilized in the present work to model the CVD of TiN on the grain scale.

In the present paper, a multi-length scale approach is used to study the CVD of polycrystalline TiN coatings. First, the CVD process is analyzed at the reactor-scale by solving the appropriate boundary value problem for a reactive gas mixture in contact with a deposition surface. In order to account for the difference between the growth rates of {111}- and {100}-oriented facets of a polycrystalline coating surface, the rates of TiN bond-breaking surface reactions are adjusted in the two cases to take into account the effect of the surface morphology. Next, atomic-scale modeling of the growth of {111}- and {100}-oriented TiN facets is carried out and coupled with the reactor-scale simulations. This coupling is achieved by using the concentrations of the gas-phase and surface species at the deposition surface resulting from the reactor-scale calculation as the boundary conditions for the atomic-scale modeling. Next, the atomic-scale and the grain-scale models are coupled in order to analyze the evolution of grain morphology and crystallographic texture during CVD of polycrystalline TiN coatings. This coupling is achieved by using the {100} and {111} surface growth rates obtained in the atomic-scale calculations, as input to the grain-scale modeling.

The organization of the paper is as following: In Section 2, a brief overview of the CVD of TiN from a TiCl₄- and NH₃-based reactive gas is presented. A brief description of reactor-scale model and its application to CVD in a hot-filament rotating-disk reactor is given in Section 3. Atomic-scale modeling of the CVD process using a kinetic Monte Carlo method is introduced and applied to the {100}- and {111}-oriented single crystalline TiN coatings in Section 4. A grain-scale model for the deposition of polycrystalline TiN coatings is presented in Section 5. The main conclusions resulted from the present work are summarized in Section 6.

2. Chemistry of CVD of TiN from TiCl₄ and NH₃

The following overall reaction for the chemical vapor deposition of TiN from TiCl₄ and NH₃ has been proposed by Larson and Allendorf [11]:



where G and D within the parentheses indicate a gas-phase or a deposited solid species, respectively. If the rate of production of TiN(D) species is denoted as r , the rate of production and consumption of the other species appearing in Equation (1) can be defined as shown in Table I. It should be noted that the Gibbs free energy change accompanying the CVD reaction, Equation (1), is highly negative at temperatures above ~ 600 K. Consequently, the CVD reaction given by Equation (1) is

TABLE I Rates of production of various gas-phase and bulk species appearing in the overall deposition reaction of TiN, Equation 1, and their relations with the rates of surface reactions

Species	Rate of production
TiN(D)	r
HCl(G)	$4r = R_1 + R_2 + R_3 + R_4 + R_5 + R_6 + R_7 + R_8 + R_9 + R_{10} + R_{11}$
N ₂ (G)	$r/6 = R_{14}$
TiCl ₄ (G)	$-r = -R_1 - R_2$
NH ₃ (G)	$-4r/3 = -R_3 - R_4 - R_5$
Ti(D)	$r = R_1 + R_2$
N(D)	$r = R_3 + R_4 + R_5 - 2R_{14}$

assumed to be irreversible at the commonly used deposition temperature (> 600 K). It should also be noted that titanium atoms undergo a change in the oxidation state from +4 to +3 during deposition. Consequently, in addition to HCl(G), molecular nitrogen N₂(G) also forms during the CVD of TiN.

Larson and Allendorf [11] also proposed a surface reaction mechanism consistent with Equation 1. The mechanism is based on the following gas-phase, surface and bulk species:

Gas: TiCl₄(G), NH₃(G), HCl(G), N₂(G);
 Surface: TiCl₃(S), TiCl₂(S), TiCl(S), Ti(S), Ti*(S), NH₂(S), NH(S), N(S), N*(S), N**(S);
 Bulk: Ti(D), N(D).

A surface species is defined to be one that resides in the topmost layer of the solid, while the bulk species reside in any layer below the topmost layer. It should be noted that Ti-N bonds are not explicitly noted in the designation for the surface and bulk species. Thus, for example, TiCl₃(S) is a surface species in which one of the original Ti-Cl bonds has been replaced by a Ti-N bond, while in Ti(S) all four of the Ti-Cl bonds have been replaced. In the case of Ti*(S), however, one of the new Ti-N bonds has been broken. The nitrogen-containing surface species are denoted in an analogous manner, so that in the case of N**(S) two of the Ti-N bonds have been broken. Since the oxidation states of Ti and N are both +3 in bulk TiN, Ti*(S) and N(S) species are the immediate precursors to a bulk titanium atom, Ti(D), and a bulk nitrogen atom, N(D), respectively. According to surface reaction S14, a N₂ molecule is formed from two N**(S) species by breaking the last Ti-N bond to each. It should be noted that whenever a nitrogen surface species loses a bond, a titanium species must do the same.

Both the gas-phase and surface species take part in surface reactions which are classified into five groups, as shown in Table II. A schematic of surface reactions S1 and S3 taking place on {100} and {111} planes is shown in Figs 1 and 2, respectively.

It should be noted that each surface reaction automatically conserves the total number of surface species, i.e. surface sites. In the case of surface reaction S1, for example, when a gas-species TiCl₄(G) attaches to the

TABLE II Gas-phase and surface reactions and the corresponding reaction rate coefficients associated with CVD of titanium nitride

No	Reaction	A_i cm-mole-s	β_i	E_i cal/mole
Nonreactive Complex Formation				
G1	$TiCl_4(G) + 2NH_3(G) \Rightarrow TiCl_4 \cdot 2NH_3(G)$	1.75×10^{18}	0.0	76000
Ti Deposition				
S1	$TiCl_4(G) + NH_2(S) + Ti^*(S) \Rightarrow TiCl_3(S) + NH(S) + HCl(G) + Ti(D)$	1.22×10^{21}	0.0	0.0
S2	$TiCl_4(G) + NH(S) + Ti^*(S) \Rightarrow TiCl_3(S) + N(S) + HCl(G) + Ti(D)$	1.22×10^{21}	0.0	0.0
N Deposition				
S3	$TiCl_3(S) + NH_3(G) + N(S) \Rightarrow TiCl_2(S) + NH_2(S) + HCl(G) + N(D)$	1.90×10^{19}	0.0	0.0
S4	$TiCl_2(S) + NH_3(G) + N(S) \Rightarrow TiCl(S) + NH_2(S) + HCl(G) + N(D)$	1.90×10^{19}	0.0	0.0
S5	$TiCl(S) + NH_3(G) + N(S) \Rightarrow Ti(S) + NH_2(S) + HCl(G) + N(D)$	1.90×10^{19}	0.0	0.0
Surface Condensation				
S6	$TiCl_3(S) + NH_2(S) \Rightarrow TiCl_2(S) + NH(S) + HCl(G)$	3.09×10^{10}	0.0	0.0
S7	$TiCl_3(S) + NH(S) \Rightarrow TiCl_2(S) + N(S) + HCl(G)$	3.09×10^{10}	0.0	0.0
S8	$TiCl_2(S) + NH_2(S) \Rightarrow TiCl(S) + NH(S) + HCl(G)$	3.09×10^{10}	0.0	0.0
S9	$TiCl_2(S) + NH(S) \Rightarrow TiCl(S) + N(S) + HCl(G)$	3.09×10^{10}	0.0	0.0
S10	$TiCl(S) + NH_2(S) \Rightarrow Ti(S) + NH(S) + HCl(G)$	3.09×10^{10}	0.0	0.0
S11	$TiCl(S) + NH(S) \Rightarrow Ti(S) + N(S) + HCl(G)$	3.09×10^{10}	0.0	0.0
Bond Breaking				
S12	$Ti(S) + N(S) \Rightarrow Ti^*(S) + N^*(S)$	8.37×10^{10}	0.0	0.0
S13	$Ti(S) + N^*(S) \Rightarrow Ti^*(S) + N^{**}(S)$	8.37×10^{10}	0.0	0.0
N ₂ Liberation				
S14	$2Ti(S) + 2N^{**}(S) + 2N(D) \Rightarrow 2Ti^*(S) + N_2(G) + N(S)$	7.00×10^{27}	0.0	0.0
Ti or N Diffusion				
S15	Diffusion on {100} atomic flat surface	1.40×10^{12}	0.0	4710
S16	Diffusion on {111} atomic flat surface	6.30×10^{13}	0.0	15600

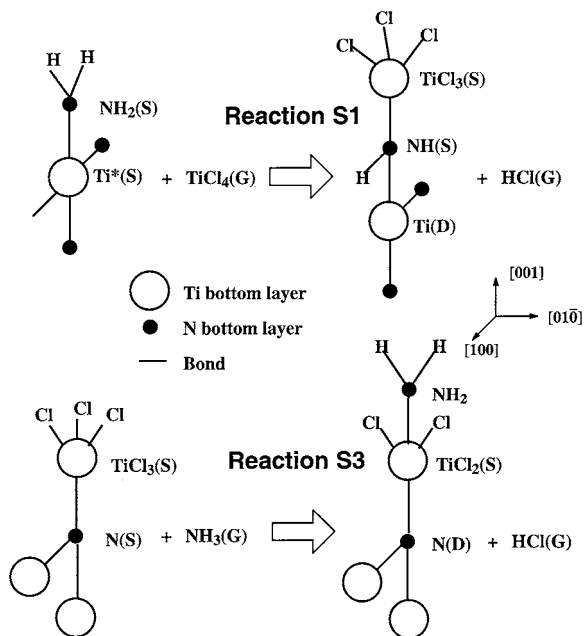


Figure 1 A schematic of the surface chemical reactions S1 and S3 (Table II) taking place during the CVD of titanium nitride on {100}-orientated substrates.

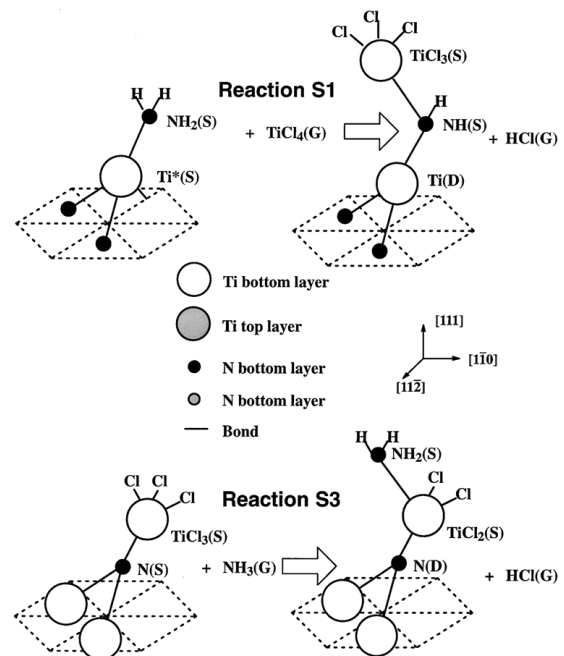


Figure 2 A schematic of the surface chemical reactions S1 and S3 (Table II) taking place during the CVD of titanium nitride on {111}-orientated substrates.

surface, a $Ti^*(S)$ becomes buried in the coating and thus becomes a bulk species, $Ti(D)$. With this interpretation, it is clear that surface reactions S1 through S5, despite the appearance of the participation of three reactants, represent essentially bimolecular processes. As a result, one bulk-phase atom is added to the solid for each one that arrives from the gas. A reverse process occurs in reaction S14.

Because the surface species are merely reaction intermediates, i.e. they do not explicitly appear in the overall deposition reaction, Equation 1, it is justified to assume that their concentrations are fixed during the

deposition process. If the rate of surface reaction i is denoted as R_i , ten conservation equations, one for each surface species, can be written, as shown in Table III. These equations can be readily understood. For example, the conservation equation for $TiCl_3(S)$ is obtained by recognizing that this surface species is generated in reactions S1 and S2 and that it is consumed in reactions S3, S6 and S7.

Since the species appearing in Equation 1 also take part in the surface reactions, their rates of production/consumption can be related to the rates of the

TABLE III Conservation equations for the surface species

Surface Species	Conservation Equations
TiCl ₃ (S)	$R_1 + R_2 = R_3 + R_6 + R_7 = r$
TiCl ₂ (S)	$R_3 + R_6 + R_7 + R_4 + R_8 + R_9 = r$
TiCl(S)	$R_4 + R_8 + R_9 = R_5 + R_{10} + R_{11} = r$
Ti(S)	$R_5 + R_{10} + R_{11} = R_{12} + R_{13} + 2R_{14} = 3R_{12} = r$
Ti*(S)	$R_{12} + R_{13} + 2R_{14} = 3R_{13} = R_1 + R_2 = r$
NH ₂ (S)	$R_3 + R_4 + R_5 = R_1 + R_6 + R_8 + R_{10}$
NH(S)	$R_1 + R_6 + R_8 + R_{10} = R_2 + R_7 + R_9 + R_{11}$
N(S)	$R_2 + R_7 + R_9 + R_{11} + 2R_{14} = R_3 + R_4 + R_5 + R_{12}$
N*(S)	$R_{12} = R_{13}$
N**(S)	$R_{13} = 2R_{14}$

appropriate surface reactions. Such relations are given in Table I.

As discussed earlier, there are ten surface species and thus that many conservation equations. However, since the total concentrations of Ti- and N-based surface species are both conserved, only eight of these equations are independent. The eight conservation equations for the first seven surface species and the last surface species, Table III, can be written as:

$$R_1 + R_2 = R_3 + R_6 + R_7 = R_4 + R_8 + R_9 = R_5 \\ + R_{10} + R_{11} = 3R_{12} = 3R_{13} = 6R_{14} = r \quad (2)$$

$$R_3 + R_4 + R_5 = R_1 + R_6 + R_8 + R_{10} \\ = R_2 + R_7 + R_9 + R_{11} = 4r/3 \quad (3)$$

In order to quantify the rates of surface reactions, Larson and Allendorf [11] assumed mass-action kinetics and that the rate constants for all the surface reactions in the same of the five groups listed in Table II, have the same value. The five rate constants are denoted as α , β , γ , λ and δ , respectively. In order to determine these rate constants, Larson and Allendorf [11] expressed the overall reaction rate, r , in terms of the concentrations of TiCl₄(G) and NH₃(G) gas-phase reactants and the five rate constants. This was done through the use of Equations 2 and 3, and the condition that the total concentrations of Ti- and N-based surface species are each equal to 0.5ϱ , i.e.:

$$C_{\text{TiCl}_3(\text{S})} + C_{\text{TiCl}_2(\text{S})} + C_{\text{TiCl}(\text{S})} + C_{\text{Ti}(\text{S})} = 0.5\varrho \quad (4)$$

$$C_{\text{NH}_2(\text{S})} + C_{\text{NH}(\text{S})} + C_{\text{N}(\text{S})} + C_{\text{N}^*(\text{S})} + C_{\text{N}^{**}(\text{S})} = 0.5\varrho \quad (5)$$

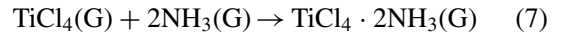
where C denotes the concentration of a given surface species and ϱ is the surface site density. In addition, the concentration of N(D) is set to 0.5 of the bulk molar density and incorporated into reaction rate constant, δ . By combining Equations 2–5, Larson and Allendorf [11] obtained the following relations:

$$r = \frac{3\lambda}{4(\phi_n + 2)^2} \left\{ \left[\frac{\lambda}{2\delta} + \varrho^2 \frac{(\phi_n + 2)\theta\phi_t\phi_n}{1 + \phi_t + \theta\phi_t\phi_n} \right]^{1/2} - \left(\frac{\lambda}{2\delta} \right)^{1/2} \right\} \quad (6)$$

where

$$\phi_t = \frac{5\alpha}{3\gamma} C_{\text{TiCl}_4} \quad \phi_n = \frac{5\beta}{4\gamma} C_{\text{NH}_3} \quad \text{and} \quad \theta = \frac{\gamma}{5\lambda}$$

In order to account for the experimentally observed small negative order of the TiN deposition rate with respect to the concentration of TiCl₄(G), a homogeneous reaction for formation of a non-reactive complex TiCl₄ · 2NH₃(G) is postulated as:



with a third-order rate constant k . Based on this reaction, as the concentration of TiCl₄(G) in the inlet gas is increased, it causes additional NH₃(G) to be tied up in the TiCl₄ · 2NH₃(G) complex. This decreases the concentration of NH₃(G) available for the CVD of TiN and, in turn, decreases the deposition rate of TiN.

Six reaction rate constants are determined by fitting the measured TiN deposition rates at 903 K [29] under different processing conditions, with the reactor-scale model predictions [30]. To account for the observed substantial temperature difference between the substrate and the inlet shower head in the reactor, an activation energy E is introduced in conjunction with the gas-phase reaction, Equation 7. Thus, the total of seven parameters: α , β , γ , λ , δ , k and E is evaluated, Table II. A surface site density $\varrho = 3.61 \times 10^{-9}$ mol/cm², computed from the bulk density of TiN, is used in the computations. It should be noted that through the use of a reactor model, Larson and Allendorf [11] managed to account for the effects of mass transport and reactant depletion on the rate of TiN deposition.

A comparison between the model predicted and measured TiN deposition rates at 903 K under the CVD processing conditions not used for parameters fitting, showed that chemistry of the CVD of TiN from TiCl₄ and NH₃ as described by Larson and Allendorf [11] is quite reasonable and hence will be used in the present work.

3. Reactor-scale modeling of the CVD of TiN coatings

In this section, the CVD of TiN coatings is analyzed by solving a reactive-gas, fluid-dynamic, heat-transfer problem at the length-scale of a CVD reactor.

3.1. Computational procedure

The reactor-scale modeling of the CVD of TiN coating is carried out for a standard rotating-disk hot-filament CVD reactor. Since we recently reported a detailed description of the reactor-scale analysis of CVD of diamond in a rotating-disk hot-filament reactor [31], only a brief description of this approach will be given in this paper. The rotating-disk hot-filament CVD reactor is a reactor in which a heated disk-shaped substrate spins in an cylindrical enclosure through which the reacting gas flows. Due to a simple geometry of the reactor, the species and temperature gradients normal to the disk are nearly equal everywhere on the disk [32]. This gives rise to a very attractive uniform distribution of

the deposition rates on the substrate and simplifies the modeling considerably.

In the present work, the method initially proposed by Evans and Greif [33] and subsequently extended by Coltrin *et al.* [34] to include the coupling between fluid flow and chemical kinetics is used to analyze the CVD process within a rotating-disk reactor. The method accounts for production/depletion of the species due to chemical reactions in the gas phase and at the substrate/coating surface and for the convective and diffusive transport of species within the gas phase and to the deposition surface. The model allows determination of surface coverages, deposition rates, gas-phase species concentration profiles, gas velocity profiles, and temperature profiles as a function of the process parameters such as the temperature and the rotation speed of the disk, reactor pressure, and inlet gas flow rates and species mass fractions.

In the present work, the rotating-disk reactor is assumed to be of an infinite radius, and to be separated in the axial direction from a parallel porous stationary heater. A forced, purely axial flow from the heater is directed toward the disk. The flow at the heater is approximated by the inlet flow conditions into the reactor. Due to the finite domain dimension in the axial direction, a radial pressure gradient is developed. The non-isothermal reacting-flow boundary value problem is defined by a set of governing steady-state partial differential equations which includes the equations for the mixture continuity, radial and circumferential momentum conservation, thermal energy and species conservation. In these equations, both convection and diffusive transport of species are considered as well as production/consumption of the species by the chemical reactions. Thermal diffusion is taken into account in the thermal energy conservation and species continuity equations. Transport properties are considered as temperature and mixture-composition dependent. Most of the boundary conditions at the heater and the substrate surface are set to their typical value: e.g. the concentrations of the gas species at the heater are set equal to their values in the input gas. Two boundary conditions at the substrate surface, however, needed special attention: (a) Due to the Stefan flow, the axial gas velocity at the substrate is defined through a mass flux matching condition at the substrate surface and; (b) the mass fractions of the gas-phase species are defined in terms of their mass flux balance.

The one-dimensional computational domain in the axial-direction between the heater and the substrate is initially divided into 20 intervals, the governing differential equations expressed at each of the internal discrete points using their finite difference form and the problem solved using the SPIN computer program [30]. This program provides an adaptive mesh refinement in the region of high gradients and thus enables a high accuracy of the solution. The solution consists of the steady-state velocity, temperature and gas species profiles in the gas-phase as well as of the steady-state surface concentrations of the surface species. In addition, the production rates of surface species, and thus the coating deposition rate is obtained.

It is well-established that at lower deposition temperatures such as 903 K, the TiN coating surface is covered with {100} facets and that the coating acquires a strong <100> texture. Based on these observations, the growth rate parameter, α , defined in Section 5, is near but slightly lower than 3.0. Then the growth velocity of {111} facets can be estimated as $V_{111} = \sqrt{3}V_{100}/\alpha$ where V_{111} and V_{100} are the growth rates of the {111} and {100} facets, respectively and α is arbitrarily set to 2.95. Since TiN coatings deposited at 903 K are covered with {100} facets nearly parallel with the substrate, the reactor-scale growth rate results can be assigned to the {100}-facet growth. The {111}-facet growth rate can be computed using the aforementioned relationship between V_{111} and V_{100} .

To explain the differences in V_{100} and V_{111} , the atomic-scale structure of TiN coating surface needs to be examined. The results presented in the next section indicated that at lower deposition temperature, such as 903 K used here, surface diffusion takes place to a substantially greater extent on {100} facets than on {111} facets. Consequently, the surface structure of {100} facets is dominated by larger islands of the new layers while in the case of {111} facets newly-deposited layers are composed predominantly of single adatoms and small clusters. These differences can play a major role in determining the extent to which the bond-breaking reactions (reactions S12 and S13) can take place. Since most surface atoms on {111} planes are present as single adatoms, reactions S12 and S13 will take place to a greater extent. This in turn, through the nitrogen liberation process described by reaction S14, will yield a lower growth rate. To account for these effects and to obtain the growth rate parameter $\alpha = 3.0$, the rate constants for reactions S12 and S13 are increased by a factor 2.02 in order to model the growth of {111} oriented facets.

3.2. Results

An example of the typical results obtained by analyzing the CVD of TiN coatings at the reactor scale is shown in Fig. 3a–d and Table IV. Fig. 3a and b show the axial

TABLE IV Mole fractions of gas-phase species (G) and site fractions of surface species at {100} and {111} surface facets. The CVD processing conditions are the same as the one stated in the caption of Fig. 3

Species	{100}	{111}
TiCl ₄ (G)	1.403×10^{-02}	1.415×10^{-02}
NH ₃ (G)	8.402×10^{-03}	8.445×10^{-03}
HCl(G)	7.295×10^{-04}	4.218×10^{-04}
N ₂ (G)	2.983×10^{-05}	1.725×10^{-05}
H ₂ (G)	9.709×10^{-01}	9.710×10^{-01}
TiCl ₄ · 2NH ₃ (G)	5.952×10^{-03}	5.984×10^{-03}
TiCl ₃ (S)	2.839×10^{-01}	2.995×10^{-01}
TiCl ₂ (S)	2.839×10^{-01}	2.995×10^{-01}
TiCl(S)	2.839×10^{-01}	2.995×10^{-01}
Ti(S)	1.458×10^{-01}	9.877×10^{-02}
Ti*(S)	2.570×10^{-03}	2.688×10^{-03}
NH ₂ (S)	5.708×10^{-02}	3.129×10^{-02}
NH(S)	5.708×10^{-02}	3.129×10^{-02}
N(S)	4.925×10^{-02}	2.686×10^{-02}
N*(S)	4.925×10^{-02}	2.686×10^{-02}
N**(S)	7.873×10^{-01}	8.837×10^{-01}

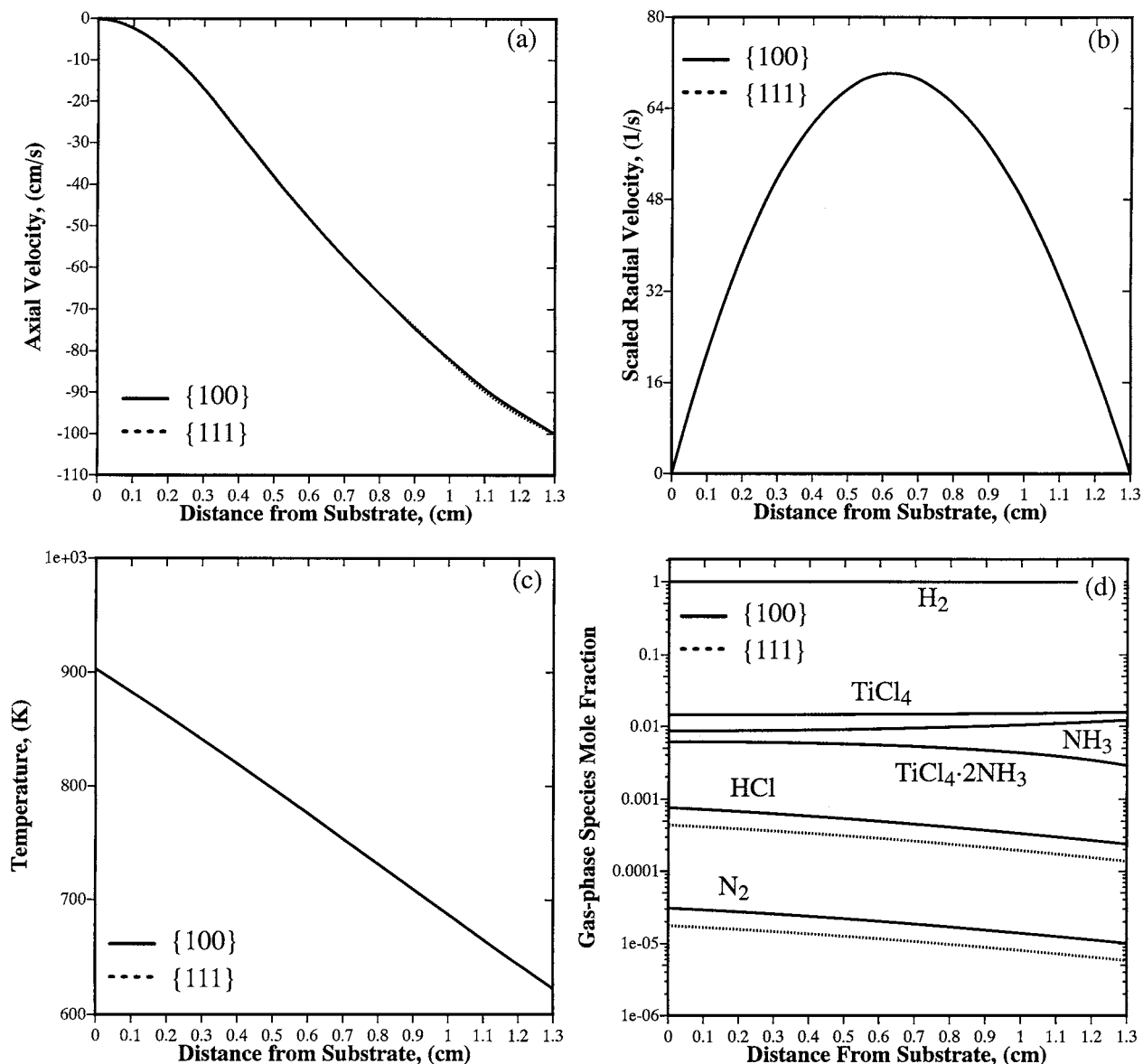


Figure 3 Axial velocity fields, (a), scaled radial velocity fields, (b), temperature fields, (c), and the gas-species concentration fields, (d), as a function of the distance from the {111}-/ {100}-oriented TiN substrate under the following CVD condition: Reactive gas at the reactor inlet (1.94% TiCl₄, 1.94% NH₃, 96.12% H₂), $T_{\text{heater}} = 623$ K, $T_{\text{substrate}} = 903$ K, $p = 20$ torr, heater-to-substrate distance = 1.3 cm.

and substrate-radius scaled radial velocity fields under the following processing conditions: Reactive gas at the reactor inlet (1.94% TiCl₄, 1.94% NH₃, 96.12% H₂), $T_{\text{heater}} = 623$ K, $T_{\text{substrate}} = 903$ K, $p = 20$ Torr, heater-to-substrate distance = 1.3 cm. Fig. 3c and d show the corresponding temperature and gas-phase species concentration fields. The concentrations of the gas-phase and the surface-species at the substrate surface are given in Table IV. The results obtained using the original values of the rate constraints for reactions S12 and S13 are denoted as {100} and the ones obtained with the modified rate constants as {111}. The results shown in Fig. 3a–d and Table IV suggest that the crystallographic orientation of the surface facet has a minor effect on the gas-phase fields but a significant effect on the concentration of the gas-phase and surface species on the facet surface. This is quite important since it is the surface concentrations and not the gas-phase fields which are used as input to the atomic-scale modeling discussed in the next section.

4. Atomic-scale modeling of the CVD of single-crystalline TiN coatings

In this section, the CVD of TiN coatings is analyzed at the atomic scale in order to determine the effect of various surface reactions on the rate of deposition, surface morphology and incorporation of the defects into the coating. Due to restrictions associated with the maximum size of the computational crystal which can be handled using the available computational resources, only the CVD of single-crystalline TiN coatings is modeled. Furthermore, since the surface of polycrystalline TiN coatings is generally faceted with {111} and {100} crystallographic planes, only {111}- and {100}-oriented single-crystalline TiN coatings are analyzed here.

4.1. Generation of the substrates

The CVD of {111}- and {100}-oriented single-crystalline TiN coatings has been modeled at the atomic

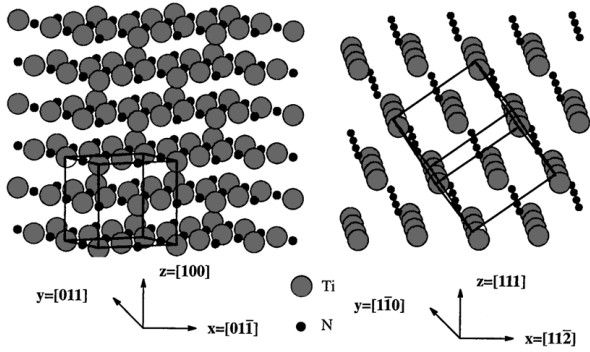


Figure 4 Portions of: (a) {100}- and; (b) {111}-oriented TiN substrates used in the atomic-scale simulation of the CVD of TiN. A TiN unit cell is delineated in each case for improved clarity.

scale within the framework of a rigid B₁-type crystal structure. This structure consists of two interpenetrating face centered cubic lattices, one occupied by Ti atoms and the other by N atoms. Within the rigid-lattice framework, local atomic relaxations and atomic vibrations are not considered. The CVD is assumed to take place on single-crystalline TiN substrates of the particular orientation. Portions of the two substrates used in the present work are shown in Fig. 4. In the case of {111}-oriented substrate, the orientation of the lattice is defined as: $x = [11\bar{2}]$, $y = [1\bar{1}0]$ and $z = [111]$ while in the case of the {100}-oriented substrate the lattice orientation is defined as $x = [011]$, $y = [01\bar{1}]$, $z = [100]$. Each coating is allowed to grow in z -direction while the periodic boundary conditions are applied in x and y directions in order to avoid coating-edge effects. The size of the computational lattice in the x - y plane is $40 d_{(112)} \times 60 d_{(110)}$ for the {111}- and $40 d_{(011)} \times 60 d_{(011)}$ for the {100}-orientated substrate where $d_{(uvw)}$ is the spacing of the (uvw) TiN planes. Initially, six {111} and six {100} planes of the TiN lattice are filled with Ti and N atoms to form two six-layer thick substrates. In the case of the {111}-oriented substrate, alternate {111} planes are filled with Ti and N atoms, while in the case of {100}-oriented substrate, each {100} plane is filled in a regular pattern with 50% Ti and 50% N atoms. In both cases the substrates contain a perfectly ordered TiN structure.

The CVD process is simulated by allowing the substrate to interact with a hot-filament-heated process-gas containing $\text{TiCl}_4(\text{G})$, $\text{NH}_3(\text{G})$, $\text{N}_2(\text{G})$ and $\text{HCl}(\text{G})$. The surface of the substrate is initially covered with the surface species listed in Table III. The concentrations of the gas-phase and surface species at the deposition surface are initially set to their values obtained via the reactor-scale modeling of the TiN CVD process, Table IV.

4.2. Surface reaction kinetics

To ensure consistency between the reactor-scale and the atomic-scale modelling schemes, the kinetics of surface reactions is treated using the same general formalism adopted in the Surface ChemKin computer program [30] which was used in the previous section. Within this formalism, the forward rate constant for reaction i , k_{f_i} , is assumed to be given by the following Arrhenius-

type relation:

$$k_{f_i} = A_i T^{\beta_i} \exp\left(-\frac{E_i}{RT}\right) \quad (8)$$

where A_i is pre-exponential factor, β_i , a temperature exponent and E_i , the activation energy. The values of these parameters for all the surface reactions associated with the CVD of TiN are given in Table II. It should be noted that according to Larson and Allendorf [11], all surface reactions are irreversible at the temperature of interest here. Hence the reverse reaction rate constants do not need to be evaluated which simplifies the analysis considerably.

Since the purpose of atomic-scale simulations, is not only to determine the rate of deposition of TiN coatings but also to reveal the evolution of the surface texture and to identify the processes which can lead to formation of defects, and since the latter phenomena are greatly affected by surface diffusion, in addition to the surface reactions listed in Table II, surface diffusion is also considered.

Surface diffusion is allowed to take place under the constraints that each species remains on its sublattice and that, as a result of an atomic jump, the number of Ti-N bonds is not reduced. A surface atom is allowed to diffuse not only on an atomically-flat surface but also between the surface planes of different altitude. The reaction rate constant for surface diffusion is assumed to be given by Equation 8, with $\beta_i = 0$. The pre-exponential term A_i and the surface-diffusion activation energy E_i are determined using the procedure discussed below.

To determine A_i and E_i for surface diffusion, it is assumed that the atomic interactions within TiN can be modeled using a Lennard-Jones 6–12 pair potential according to which the potential energy of the crystal is given as:

$$E = \frac{1}{2} \sum_{i,j \neq i} \phi_{\alpha\beta}(r_{ij}) \quad (9)$$

where the pair potential $\phi_{\alpha\beta}$ is defined as:

$$\phi_{\alpha\beta}(r_{ij}) = \begin{cases} 4\varepsilon_{\alpha\beta} \left[\left(\frac{\sigma_{\alpha\beta}}{r_{ij}} \right)^{12} - \left(\frac{\sigma_{\alpha\beta}}{r_{ij}} \right)^6 \right], & 0 < r_{ij} < \frac{a\sqrt{5}}{2} \\ 0, & r_{ij} \geq \frac{a\sqrt{5}}{2} \end{cases} \quad (10)$$

α and β are respectively the species of atoms i and j , r_{ij} is the distance between atoms i and j , and a is the TiN lattice parameter ($a = 0.424$ nm [2]). The $\phi_{\text{Ti-Ti}}$ and $\phi_{\text{N-N}}$ interatomic potential are taken from our previous work [35, 36]. The $\phi_{\text{Ti-N}}$ interatomic potential is obtained by requiring that the minimum of E given by Equation 9 for a bulk crystal corresponds to the Ti-N binding energy of 454.8 eV [37] and that it is associated with the Ti-N nearest neighbor distance equal to $a/2$.

The rate parameters A_i and E_i are determined using a simple case in which a single atom (adatom) is residing on a rigid atomically flat surface. The potential energy of such a configuration is a function of the coordinates of the adatom alone. Since the atoms on the atomically flat surface are fixed, the in-plane (x , y) coordinates of the adatom corresponding to its equilibrium (minimum-energy) and its instability (saddle-point) configurations can be determined by geometrical considerations. Then the z coordinate of the adatom associated with the two configurations and the corresponding energies E_{\min} and E_{saddle} are determined by finding the minimum of the potential energy function given by Equation 9 relative to the z coordinate of the adatom. The activation energy E_i for surface diffusion is next set equal to $E_{\text{saddle}} - E_{\min}$. To compute the pre-exponential term A_i for surface diffusion, the procedure proposed by Voter [38] is followed. According to this procedure, a 3×3 matrix containing second-order derivatives of the potential energy E is derived by differentiating twice Equation 9 with respect to the coordinates of the adatom. Next, the matrix is evaluated at the equilibrium and the saddle-point coordinates of the adatom and the eigenvalue of the two resulting matrices determined. For each eigenvalue b_i , the corresponding vibrational frequency is computed as:

$$v_i = \frac{1}{2\pi} (b_i/m)^{\frac{1}{2}} \quad (11)$$

where m is the mass of a Ti or a N atom. Lastly, the pre-exponential term A_i is computed as:

$$A_i = \frac{v_{1m} v_{2m} v_{3m}}{v_{2s} v_{3s}} \quad (12)$$

where v_{1m} , v_{2m} , and v_{3m} are the three vibrational frequencies associated with the minimum-energy position of the adatom and v_{2s} and v_{3s} the two non-imaginary frequencies corresponding to the saddle-point location of the adatom.

The values for the pre-exponential term A_i and the activation energy E_i for surface diffusion of a Ti and a N adatom on atomically flat {100} and {111} surfaces obtained using the aforementioned procedure are listed in Table II.

4.3. Simulation procedure

The temporal evolution of single-crystalline TiN coatings during the CVD is modeled using the version of the kinetic Monte Carlo method recently developed by Battaile *et al.* [24]. Within this method, one surface reaction is allowed to take place at one surface site during each time step. The occurrence of one of the reactions at one of the sites is termed an event. At each time step, a list of all possible events is constructed and the probability for each event is set equal to the ratio of the rate of the associated surface reaction and the sum of the rates of surface reactions associated with all the other possible events. Then an event is selected at random and allowed to take place. After the event has occurred, the total number of possible events, and the sequence

in which the events are listed are updated and the aforementioned procedure is repeated.

The present Monte Carlo method uses a variable time step which is adjusted dynamically and stochastically to accommodate the fastest possible event which requires the smallest time increment. This greatly reducing restrictions associated with conventional fixed time-increment Monte Carlo methods. A more comprehensive overview of the kinetic Monte Carlo method used in the present study can be found in our recent publication [25].

4.4. Analysis of surface crystal defects

During the growth of {111}-oriented single-crystalline TiN coatings, various crystal defects of the point, line and planar type can form. The most frequent point-type defects are vacancies and entrapped hydrogen and chlorine atoms. Partial dislocation loops (line defects) with the Burgers vector $\mathbf{b} = a/6\langle 1\bar{2}1 \rangle$ which encircle {111}-type twins (planar defects) can also form during the growth of {111}-oriented TiN coatings. Point-type defect also form during the deposition of {100}-oriented TiN coatings. However, formation of line and planar defects in this case is less likely. The atomic-scale simulation method used in the present work enables identification of the defect generation mechanisms and monitoring of the defect content in coatings during the deposition process.

4.5. Results

An example of the atomic-scale simulation results for the CVD of TiN single crystalline coatings with {100} and {111} crystallographic orientation is shown in Figs 5 and 6, respectively. The coatings are processed under the CVD conditions identical to the ones associated with the reactor-scale results shown in Fig. 3 and the ones which correspond to the growth-rate parameter $\alpha = 2.95$.

The top view of a {100}-oriented TiN coating at two different deposition times is shown in Fig. 5a and b. To denote the altitude of the deposited atoms relative to the substrate, different shades of gray are used. The brightest shade of gray denotes atoms in the top-most surface

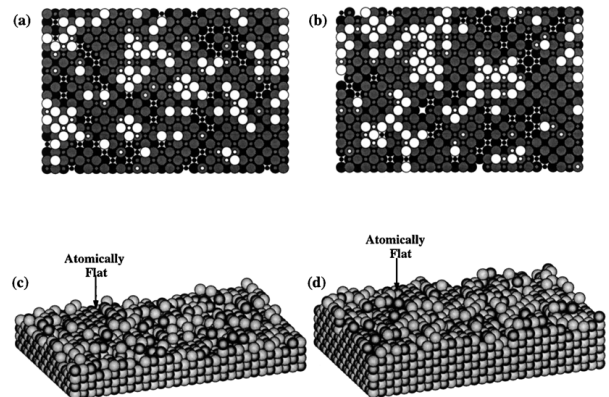


Figure 5 (a) and (b) top and (c) and (d) side views of a {100}-oriented TiN coating after: (a), (c) 0.016 and (b), (d) 0.051 sec of simulation time. See text for details of the process parameters.

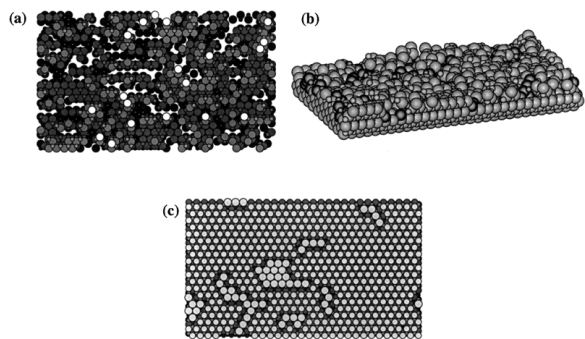


Figure 6 (a) Top and (b) side views of a {111}-oriented TiN coating after 0.108 sec of simulation time. (c) A section of coating parallel to the substrate surface reveals the presence of twinned regions (larger balls). See text for details of the process parameters.

layer. Also different sizes of balls are used to represent Ti (large balls) and N (small balls) atoms. To further improve the clarity, only the atoms in the top four surface layers are shown. The deepest surface troughs are found to be six layers deep. The results displayed in Fig. 5a and b show that the coating surface contains islands of the new layers scattered over atomically-flat regions of fully-filled layers. This suggests that surface diffusion, which enables isolated adatoms to move over the coating surface until they attach themselves to an island, has an important effect on the surface morphology in {100}-oriented coatings. A comparison of the results at two different simulation times, Fig. 5a and b, suggests that this basic surface morphology is maintained during the deposition process. Fig. 5c and d show side views of the {100}-oriented TiN coatings, whose top view is displayed in Fig. 5a and b, respectively. The side views provide an additional visual insight into the morphology of the coating surface described above. To improve clarity, Ti and N atoms in Fig. 5c and d are represented by same-size balls but of different shading.

A top view and the corresponding side view of a {111}-oriented TiN coating whose deposition is simulated under the identical CVD conditions as that of its {100}-oriented counterpart are shown in Fig. 6a and b, respectively. Again, only four top surface layers are represented. The deepest surface troughs are found to be 10 layers deep. These troughs appear as voided areas in Fig. 6a. Clearly in comparison to the {100}-oriented coating, the surface of the {111}-oriented TiN coating is quite irregular at the atomic-scale and it remains such during the deposition process (the results at different deposition times not shown for brevity). This finding is consistent with the fact that the diffusion coefficient for Ti and N at {111} crystallographic planes is only about 5% of their values at {100} crystallographic planes at 903 K. Consequently, Ti and N adatoms show very little mobility on {111}-crystallographic planes and no significant formation of islands takes place. Fig. 6c shows an atomic arrangement obtained by cutting the coating parallel to the substrate. Large balls are used to indicate atoms which reside in twin positions. It should be noted that in its present formulation, surface diffusion does not allow exchange of adatoms between the regular and the twinned sublattices. This limitation of the

current model can explain the linear and branched geometry of the observed microtwins which is energetically less favored.

The effect of the nitrogen-to-titanium molar ratio (under a constant NH_3 concentration condition) in the feed gas, $m_{\text{N/Ti}}$, on the deposition rate of {100}-oriented TiN coatings at 903 K is shown in Fig. 7a. Both the reactor-scale and the atomic-scale results are displayed. For comparison, experimental results of Custer and Smith [29] are also shown in Fig. 7b. The three sets of results are in relatively good mutual agreement. It should be noted, however, that the experimental results displayed in Fig. 7a were fitted to the reactor-scale model predictions by Larson and Allendorf [11] in order to determine the kinetic parameters of various surface reactions. This can explain significantly better agreement between the reactor-scale predictions and the experiment in comparison to the atomic-scale prediction.

The effect of the nitrogen-to-titanium molar fraction ratio, $m_{\text{N/Ti}}$, on the growth rate parameter α is shown in Fig. 7b. Both the reactor-scale and the atomic scale results are shown. The two sets of results show that α decreases as $m_{\text{N/Ti}}$ is increased between 0.5 and ~ 100 . Even the rate of change of α with $m_{\text{N/Ti}}$ is quite similar in the two cases. However, the atomic-scale α values are consistently higher than their reactor-scale counterparts by about 0.25–0.35. Since a similar discrepancy exists in the deposition rate results, Fig. 7a, the discrepancies can be attributed to the effect of surface diffusion which was accounted for in different ways in the two sets of calculations. In the reactor-scale calculations, surface diffusion was incorporated implicitly by modifying the appropriate reaction-rate constants. In the atomic-scale calculations, on the other hand, surface diffusion was accounted for explicitly by treating it as another surface reaction. In addition, the surface diffusion parameters were assessed using a simple model for migration of isolated adatoms on an atomically flat rigid surface. Surface relaxation effects and motion of smaller adatom clusters, which are neglected in the present model, can have a significant effect on surface diffusion [38].

The experimental results of Jiang *et al.* [54] show that at the $m_{\text{N/Ti}}$ values less than 1.0, the coating surface is covered with {100} facets, and has a near <100> texture, which, as will be shown in next section, requires an α value less than but near 3.0. Since atomic-scale results displayed in Fig. 7b show α values substantially higher than 3.0 in this $m_{\text{N/Ti}}$ range, only the reactor-scale α vs. $m_{\text{N/Ti}}$ results, Fig. 7b, will be used for the grain scale analysis in the next section. It should be noted that for the $m_{\text{N/Ti}}$ range analyzed here, α changes between 2.98 and 2.01. As will be demonstrated in the next section, this finding has an important effect on the crystallographic texture and the character of surface facets which develop in polycrystalline TiN coatings.

Fig. 8a shows the effect of the nitrogen-to-titanium molar ratio on the concentration of Cl and H atoms embedded in the {100}-oriented TiN coating. As $m_{\text{N/Ti}}$ increases, i.e. as the concentration of TiCl_4 is reduced in the feed gas, fewer Cl atoms become entrapped by the growing coating surface. Meanwhile, the concentration of embedded H atoms remains practically unaffected by

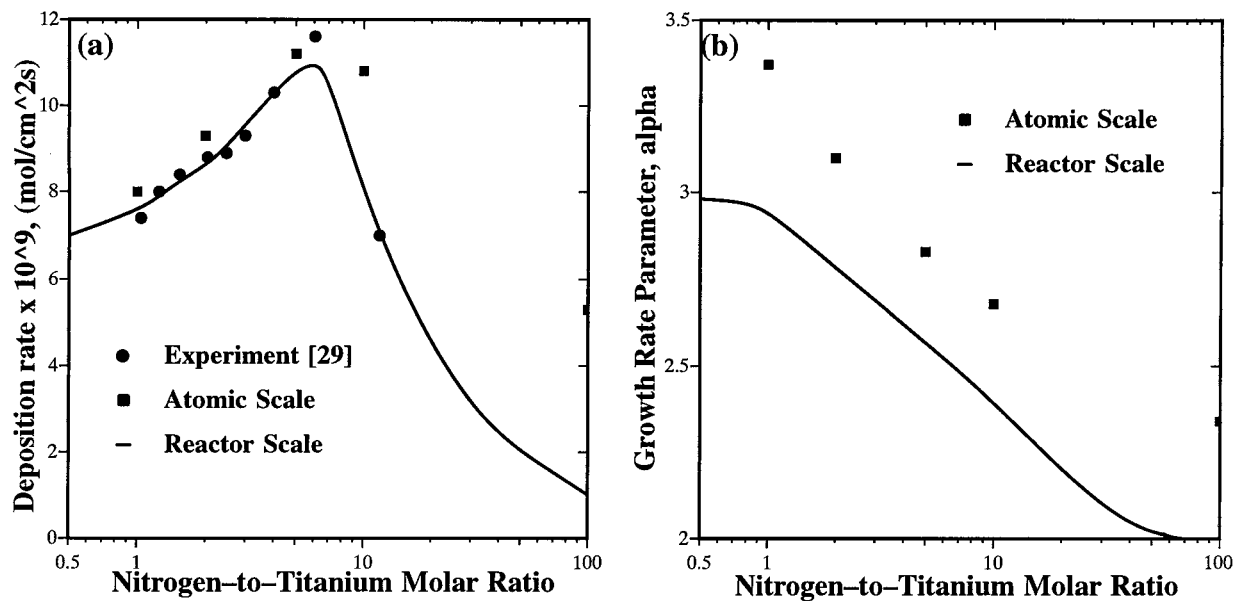


Figure 7 The effect of the nitrogen-to-titanium mole-fraction ratio, $m_{N/Ti}$, on: (a) the deposition rate of {100}-oriented TiN coatings and (b) the growth-rate parameter, α ($T_{\text{substrate}} = 903$ K).

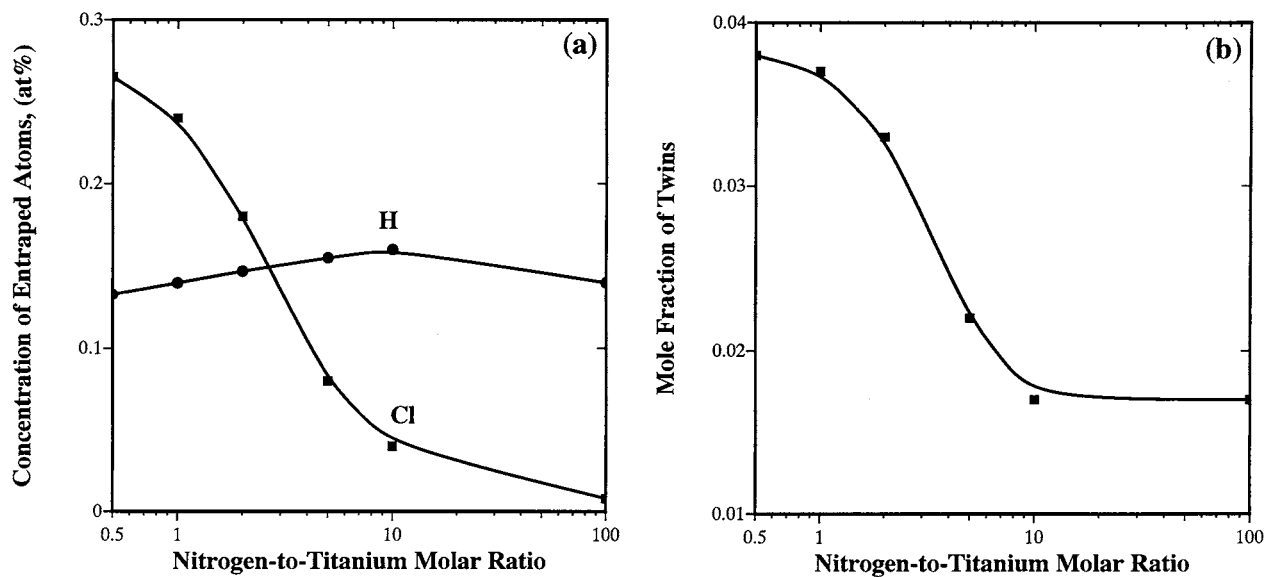


Figure 8 The effect of the $m_{N/Ti}$ ratio on: (a) the concentration of point defects in {100}-oriented TiN coatings and: (b) the volume-fraction of twins in {111}-oriented TiN coatings.

the change in $m_{N/Ti}$ which is consistent with the fact that the concentration of NH_3 in the feed gas is kept constant. The main mechanism for embedding Cl and H atoms in the coating is found to be the movement of adatoms from a higher surface position to a neighboring lower surface position, which traps the Cl- and H-bearing surface species beneath. This may explain why embedded Cl and H atoms are found only occasionally in {111}-oriented TiN coating in which the surface diffusion is quite limited.

The effect of $m_{N/Ti}$ ratio of the volume fraction of twins in the {111}-oriented TiN coating is shown in Fig. 8b. It is seen that in the $m_{N/Ti}$ range examined, an increase in $m_{N/Ti}$ from 0.5 to 100 causes the volume fraction of twins to decrease to about half of its value. A preliminary analysis of this phenomenon indicates quite complex relationships between the concentrations of the (coating) surface species and twin formation.

The results of this analysis will be reported in a future communication.

5. Grain-scale modeling of the CVD of TiN coatings

5.1. General consideration

In this section, the CVD of polycrystalline TiN coatings at the grain scale is analyzed using a Van der Drift-type model [46]. It is well-established that the surface of polycrystalline TiN coatings is faceted with the {111} and {100} crystallographic planes [e.g. 2]. While these facets are generally at an angle relative to the substrate surface, to a first order of approximation, their growth rates are expected to be comparable with the growth rates of the corresponding single-crystalline TiN coatings presented in the previous section. Hence the growth rates obtained at the atomic scale can be used as input

for a grain-scale simulation of the CVD of TiN coatings. Grain-scale simulations allow not only the growth rates of polycrystalline coatings to be predicted but also the evolution of surface structure, morphological and crystallographic texture, etc. to be monitored during deposition.

Many factors such as surface diffusion, grain boundary migration, growth competition, twinning, etc. affect the development of microstructure, defect content and morphological and crystallographic texture in CVD-grown polycrystalline coatings. When the coatings are grown at a relatively low temperature, as in the case in the present analysis, the coating microstructure is, for the most part, inherited from its surface during the deposition. As discussed in the previous section, surface diffusion can affect atomic-scale structure of the coating facets. However, the grain-scale microstructure is expected to be controlled by growth competition and, to a lower extent, by twinning. Growth competition is governed by the relative growth rates of various facets of the coating surface, while twinning is controlled by the magnitude of the stacking-fault energy and the processing stresses. The effects of both growth competition and twinning on the microstructure of polycrystalline coatings have been studied extensively [e.g. 28]. Recently, Paritosh *et al.* [26] performed a comprehensive computer simulation study of growth competition in two-dimensional polycrystalline coatings. The work of Paritosh *et al.* [26] clearly shows that growth competition has a major effect on grain size evolution and its distribution, surface roughness, morphological and crystallographic texture, and the volume fraction of the coating resulting from the growth of facets of different crystallographic orientations. However, since Paritosh *et al.* [26] analyzed a hypothetical two-dimensional polycrystalline coating, it is difficult to correlate their results with the experimental ones for the CVD-grown TiN coatings. This limitation is overcome in the present work by introducing a set of nuclei whose crystallographic features are derived from the corresponding three-dimensional characteristic shapes of isolated TiN single crystals. While the growth of polycrystalline coatings is still modeled using a two-dimensional approach, the model predictions can be more directly correlated with their experimental counterparts. In our recent work [28], it was shown that twinning can have a significant effect on the evolution of surface morphology and microstructural and crystallographic texture in polycrystalline diamond coatings. While similar effect of twinning can be expected in the case of the CVD-grown TiN coatings, to simplify the analysis such effects are not considered in the present work.

The shape of a single crystallite growing without competition from other crystallites is determined by the relative velocities of various crystallographic surfaces. The characteristic shape of a crystal growing under certain conditions, generally referred to as the idiomorph. The idiomorphs are controlled by crystallographic planes which grow at a lowest speed. In the case of TiN, such planes are of the {111} and {100} type. Wild *et al.* [44, 47] were the first to recognize that the

crystallographic texture of the polycrystalline coatings can be understood by identifying the fastest-growth direction in the corresponding idiomorph. To explain the texture of polycrystalline coatings as a function of the relative growth rates of the {100} and {111} facets, Wild *et al.* [44, 47] introduced a growth-rate parameter as:

$$\alpha = \frac{\sqrt{3}V_{100}}{V_{111}} \quad 0 \leq \alpha < \infty \quad (13)$$

where V_{100} and V_{111} are the growth rates of the {100} and {111} facets, respectively. The effect of the magnitude of α on the {100}/{111}-based TiN idiomorphs is shown in Fig. 9. For $\alpha \leq 1$ cubic idiomorphs with {100} facets are obtained. For values of $\alpha \geq 3$, the idiomorphs are perfect octahedrons bounded by {111} faces. At the intermediate values of α , cubo-octahedral crystals bounded by both {100} and {111} facets are obtained.

Wild *et al.* [44, 47] postulated and Paritosh *et al.* [26] and Grujicic and Lai [28] confirmed by computer modeling that crystallographic texture in polycrystalline coatings is dominated by the fastest-growth directions of the idiomorph. This was also confirmed experimentally [e.g. 44–47]. The Miller indices of the fastest growth direction are defined as:

$$\begin{aligned} [h \ k \ l] \\ = [\cos \phi_{\max} \sin \theta_{\max} \quad \sin \phi_{\max} \sin \theta_{\max} \quad \cos \theta_{\max}] \end{aligned} \quad (14)$$

where θ_{\max} and ϕ_{\max} are the two polar angles between the fastest-growth direction and the crystal cubic axes

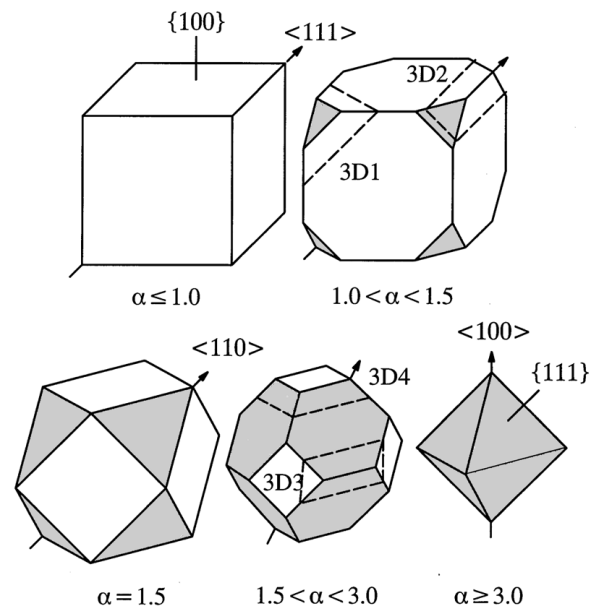


Figure 9 Idiomorphic shapes based on {100} and {111} facets for various values of the growth-rate parameter α . The arrows indicate the direction of the fastest growth. Sections marked by dashed lines are used to form the three-dimensional nuclei shown in Column 1, Table V.

and they are defined as:

$$\theta_{\max} = \begin{cases} \tan^{-1}(\sqrt{2}) & \alpha \leq 1 \\ \tan^{-1}\left(\frac{\sqrt{5\alpha^2 - 12\alpha + 9}}{\alpha}\right) & 1 \leq \alpha \leq 3/2 \\ \tan^{-1}\left(\frac{3 - \alpha}{\alpha}\right) & 3/2 \leq \alpha \leq 3 \\ 0 & 3 \leq \alpha \end{cases}$$

$$\phi_{\max} = \begin{cases} \frac{\pi}{4} & \alpha \leq 1 \\ \tan^{-1}\left(\frac{3 - 2\alpha}{\alpha}\right) & 1 \leq \alpha \leq 3/2 \\ 0 & 3/2 \leq \alpha \end{cases} \quad (15)$$

5.2. Computational procedure

The growth of polycrystalline TiN coatings at the grain scale is analyzed in the present work using the van der Drift approach [46]. Within this approach, all TiN nuclei are assumed to form simultaneously on the substrate and to grow as a result of the normal growth of each of its facets at fixed, prescribed velocities. No formation of additional nuclei is allowed during the deposition. All the nuclei of the same type are identical in every respect except for their orientation with respect to the substrate. At the very beginning of a simulation run, nuclei are generated at the substrate at random and then they are allowed to grow. Initially, the nuclei grow in isolation but, after some time, they begin to impinge on each other, ultimately forming a continuous polycrystalline coating. Grain boundaries are formed when the adjacent grains make contact with each other. No migration of the grain boundaries is considered. However, they are allowed to extend as the contacting grains continue to grow. In other words, the grain boundaries simply represent the trace of the points on the prior coating surface where the adjacent grains were contacting.

As mentioned earlier, the surface of polycrystalline TiN coatings is typically bounded by {100} and {111} crystallographic planes. Furthermore, it is well established [e.g. 48] that depending on the processing conditions a TiN coating can achieve either a (100), a (110), or a (111) crystallographic texture. As indicated by the arrows in Fig. 9, (100), (110) and (111) become the crystallographic directions of the fastest growth for $\alpha \geq 3.0$, $\alpha = 1.5$, and $\alpha \leq 1.0$, respectively. To examine the tendency of polycrystalline TiN coatings for formation of either of the three crystallographic textures listed above, three-dimensional nuclei (Column 1, Table V) are considered in the present work. These nuclei are obtained by making the appropriate sections (dashed lines in Fig. 9) of the idiomorphs corresponding to the α values of: slightly greater than 1.0, slightly lower than 1.5, slightly greater than 1.5 and slightly lower than 3.0, respectively. Next, appropriate sections of the four three-dimensional nuclei (dashed lines in

Column 1, Table V) are made to obtain seven types of two-dimensional nuclei (Column 2, Table V). Finally, for each vertex of a nucleus, the x - and y -velocity components are computed from the known growth velocities of the adjoining facets using the procedure recently devised by Grujicic and Lai [27]. The term vertex is used to denote either the point of intersection of two edges of a nucleus/grain or a point where the edges of two adjacent nuclei/grains meet. The x - and y -velocity components for the grain-boundary vertices are also determined from the known growth velocities of the adjoining facets using the aforementioned procedure.

At the beginning of a simulation run, nuclei are placed randomly on the substrate. Each nucleus/grain is completely defined by a set of vectors which specifying its orientation, location of the vertices, velocities of the adjoining facets, and the position of its origin. For each vertex, the x - and y -components of the velocity (v_x and v_y) are determined from the velocities of the neighboring facets and the coordinates of the vertices updated by adding respectively $v_x \Delta t$ and $v_y \Delta t$ to their current x - and y -coordinates, where Δt is a small time increment. While the facets orientations are fixed by the nuclei grain orientation, the position and the presence/absence of the vertices changes during the film growth. When two vertices intersect in the course of coating growth, the edge between them and one of the vertices are removed and the velocity of the remaining vertex updated using growth velocities of the newly adjacent facets. An adaptive scheme for determination of the time increment is used which allows Δt to be large enough to reduce the computation time and yet be fine enough to ensure that vertex-intersection processes are not skipped.

Because of a large number of nucleus types and the random nature of their size, position and orientation, a relatively large number (360) of nuclei were used. To improve statistics, the results reported in the next section represent the average of five runs.

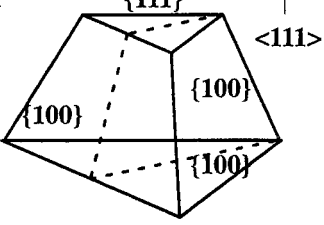
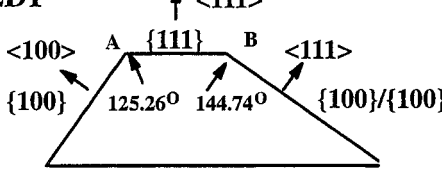
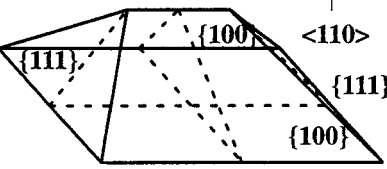
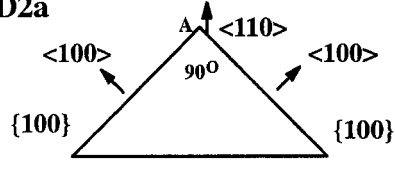
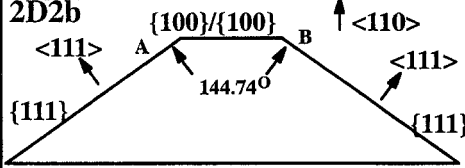
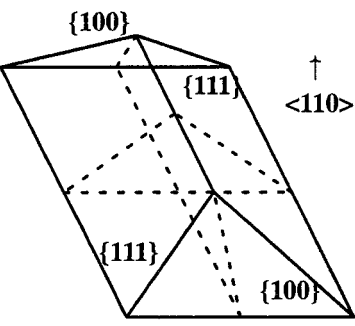
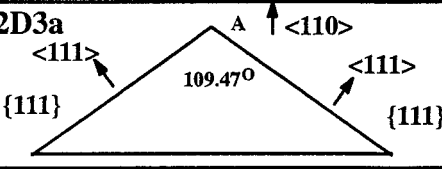
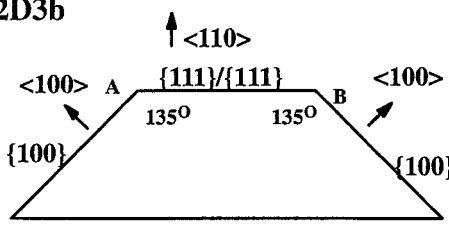
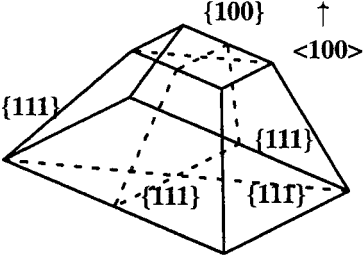
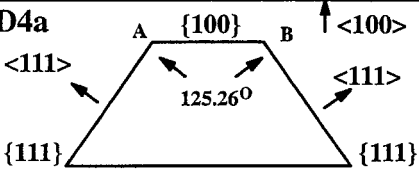
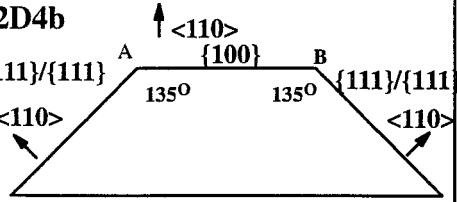
5.3. Results

The reactor-scale results shown in Fig. 7b indicate that when the nitrogen-to-titanium molar ratio, $m_{N/Ti}$, is varied between 0.5 and 100, the growth-rate parameter, α , changes between 2.98 and 2.01. Therefore, the grain-scale simulations of the CVD of TiN coatings are carried out in the present work only for the two limiting values of the growth-rate parameter: $\alpha = 2.98$ and $\alpha = 2.01$.

Fig. 10a and b show the temporal evolution of the coating surface and the location of the grain boundaries in the coating deposited under these two values of the growth-rate parameter, respectively. In both cases, the grain size increases and the grains become increasingly columnar with increasing coating thickness. Columnar-grain structure is a common feature of the CVD-grown polycrystalline TiN coatings [e.g. 49].

The film microstructure for the $\alpha = 2.98$ case, Fig. 10a, reveals surface morphology with a relatively low level of surface roughness. Further, inspection of Fig. 10a reveals that the film surface is dominated by

TABLE V The relationship between three and two-dimensional nuclei and the crystallographic features and vertex velocities of the two-dimensional nuclei

3D Nuclei	2D Nuclei	
Properties	Properties	Vertex Velocities
3D1 	2D1 	$V_x^A = -\frac{\sqrt{6}}{2}\left(1 - \frac{1}{\alpha_{3D}}\right)V_{100}$ $V_y^A = -\frac{\sqrt{3}}{\alpha_{3D}}V_{100}$ $V_x^B = -\sqrt{6}\left(1 - \frac{1}{\alpha_{3D}}\right)V_{100}$ $V_y^B = -\frac{\sqrt{3}}{\alpha_{3D}}V_{100}$
3D2 	2D2a 	$V_x^A = 0$ $V_y^A = \sqrt{2}V_{100}$
	2D2b 	$V_x^A = \left(2 - \frac{3}{\alpha_{3D}}\right)V_{100}$ $V_y^A = \sqrt{2}V_{100}$ $V_x^B = -\left(2 - \frac{3}{\alpha_{3D}}\right)V_{100}$ $V_y^B = \sqrt{2}V_{100}$
3D3 	2D3a 	$V_x^A = 0$ $V_y^A = \frac{3\sqrt{2}}{2} \frac{1}{\alpha_{3D}} V_{100}$
	2D3b 	$V_x^A = \frac{\sqrt{2}}{2}\left(\frac{3}{\alpha_{3D}} - 2\right)V_{100}$ $V_y^A = \frac{3\sqrt{2}}{2} \frac{1}{\alpha_{3D}} V_{100}$ $V_x^B = -\frac{\sqrt{2}}{2}\left(\frac{3}{\alpha_{3D}} - 2\right)V_{100}$ $V_y^B = \frac{3\sqrt{2}}{2} \frac{1}{\alpha_{3D}} V_{100}$
3D4 	2D4a 	$V_x^A = \frac{\sqrt{2}}{2}\left(\frac{3}{\alpha_{3D}} - 1\right)V_{100}$ $V_y^A = V_{100}$ $V_x^B = -\frac{\sqrt{2}}{2}\left(\frac{3}{\alpha_{3D}} - 1\right)V_{100}$ $V_y^B = V_{100}$
	2D4b 	$V_x^A = \left(\frac{3}{\alpha_{3D}} - 1\right)V_{100}$ $V_y^A = V_{100}$ $V_x^B = -\left(\frac{3}{\alpha_{3D}} - 1\right)V_{100}$ $V_y^B = V_{100}$

{100} facets (solid lines) and that it also contains several {111}/{111} facets (three-dot space lines). All the grains reaching the coating surface are associated with the nuclei of the types 2D4a and 2D4b. Since <100> is the characteristic directions for these types of nuclei, and the direction of fastest growth, <149 0 1>, is less than 1 degree off <100>, the coating acquires

a near <100> texture. The grain boundaries (dash and dot lines) are all straight and only occasionally undergo an abrupt change of their slope. These changes are associated with the merging of non-grain-boundary and grain-boundary vertices and the corresponding change in the direction and magnitude in the velocity of the remaining grain-boundary vertices.

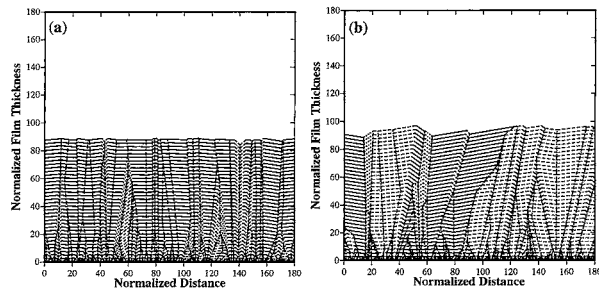


Figure 10 The microstructure of polycrystalline TiN coatings deposited under the following values of the growth-rate parameter, α : (a) 2.98 and (b) 2.01. Both the x - and the y -axis are normalized with respect to the average nucleus spacing, d_0 . The following line-type nomenclature is used: dash-dot = grain boundaries, solid = $\{100\}$ facets, dotted = $\{111\}$ facets, dashed = $\{100\}/\{100\}$ facets, and three-dot space = $\{111\}/\{111\}$ facets.

The surface morphology of a coating grown under the $\alpha = 2.01$ condition is shown in Fig. 10b. Inspection of Fig. 10b reveals that the coating surface is completely covered by $\{100\}$ facets (solid lines), $\{111\}$ facets (dotted lines) and $\{111\}/\{111\}$ facets (three-dot space line). Furthermore all the grains reaching the coating surface are associated with the nuclei of types 2D3a, 2D3b and 2D4a. While nuclei of the type 2D2b contain $\{100\}/\{100\}$ facets, these facets shrink and eventually disappear as the coating thickens. As a result, nuclei of the type 2D2b are converted into nuclei of the type 2D3a. Since $\langle 110 \rangle$ is the characteristic direction in 2D3a and 2D3b nuclei and $\langle 100 \rangle$ is the characteristic direction for 2D4a nuclei, the coating texture is represented by a direction which is between $\langle 110 \rangle$ and $\langle 100 \rangle$ directions. This direction, (67330) which is only 0.34 degrees away from $\langle 210 \rangle$, corresponds to the fastest-growth direction of the respective idiomorph.

The results shown in Fig. 10a and b indicate that the grain size increases with increasing coating thickness. After plotting the logarithm of the average grain size, \bar{d} (defined as the average width of columnar grains) and the logarithm of coating thickness, h , both normalized with respect to the average nucleus spacing, d_0 , for both values of α (the plot not shown for brevity), the following \bar{d} vs. h relationship is established:

$$\bar{d} = C_1(\alpha)h^n \quad (16)$$

where the parameter C_1 is dependent on the magnitude of the growth-rate parameter α , while the exponent n is found to be essentially independent of α and in the range between 0.49 and 0.58. The value of $n \approx 0.5$ has also been obtained in a number of both theoretical [50–52] and experimental [53] studies. It should be noted that since within the present simulation scheme, the rate of coating thickening is time independent, the coating thickness, h , and the deposition time, t , are equivalent variables and hence the average grain size shows an analogous power-law dependence on the deposition time as on the coating thickness, Equation 16.

The coating microstructure evolution results shown in Fig. 10a and b, are used to determine the grain size

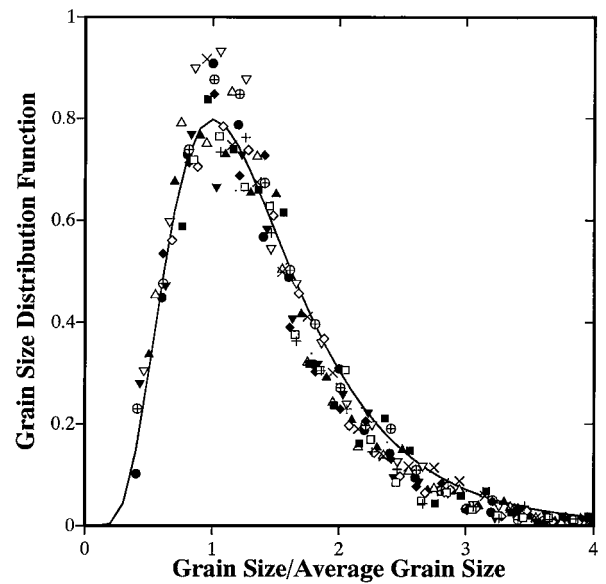


Figure 11 The distribution function for the grain size normalized with respect to the corresponding average grain size, \bar{d} , at two α values and seven coating thicknesses.

distribution and its evolution in the course of coating growth. Such distribution is found to possess the following basic features: it is nearly zero at small grain size, increases relatively fast, goes through a peak and ultimately decreases gradually toward zero at large grain size. The distribution becomes broader and its peak value decreases and shifts toward larger grain size as the coating thickens. These findings are consistent with the fact that the average grain size increases with coating thickness. The basic shape of the grain size distribution is retained as the coating grows. The distribution of a normalized grain size $d/\bar{d}(h)$ ($\bar{d}(h)$ is the average grain size at the coating thickness h) is plotted in Fig. 11 for several film thicknesses and two α values. Despite a relatively large scatter, the results shown in Fig. 11 suggest that the grain size distribution is effectively temporally self-similar and α -invariant. The results shown in Fig. 11 are fitted to a log-normal distribution in the form:

$$P[d/\bar{d}(n)] = \frac{1}{\sigma\sqrt{2\pi}} \exp\{-[\ln(d/\bar{d}(h))]^2/2\sigma^2\} \quad (17)$$

where σ is the standard deviation. The best fit of the results shown in Fig. 11 is obtained with σ in the range between 0.49 and 0.51. Paritosh *et al.* [26] showed that the simulation results of two-dimensional grain-growth in CVD-grown coatings can be more accurately fitted using a gamma distribution function. However, since no physical basis can be attributed to this type of distribution function, the results obtained in the present work are not fitted to the gamma distribution function.

As evidenced by the results shown in Fig. 10a and b, due to the faceted nature of these surface, the coatings are inherently rough. Further examination of the results shown in Fig. 10a and b indicates that the surface roughness increases with the coating thickness. By plotting the variation of the logarithm of the root-mean-square (r.m.s.) average roughness R with the logarithm

of coating thickness, both normalized with respect to be average nucleus spacing, d_0 , (results not shown for brevity) the following relationship is established:

$$R = C_2(\alpha)h^m \quad (18)$$

where the parameter C_2 is α -dependent while the exponent m is independent of α and in the range between 0.46 and 0.59. This finding suggests that the variations of both the average grain size and the r.m.s. average surface roughness with the coating thickness (deposition time) are governed by the same type of power-law relations. This finding can be readily understood since for a given crystallographic orientation of a grain, the type of surface facets is unchanged as the grain grows while their size which controls surface roughness scales with the grain size. It should be pointed out that the R vs. h relationship defined by Equation 18 is found not to be obeyed at small coating thickness which can be attributed to the fact that, at a small coating thickness, growth of a coating involves numerous events of growth-dominating grains blocking off the growth of other grains. Only after the coating surface is composed entirely of the grains originating from the rate-controlling nuclei, the R vs. h relation becomes consistent with Equation 18.

The crystallographic texture in as-grown polycrystalline TiN coatings as a function of the nitrogen-to-titanium molar ratio is shown in Fig. 12. The texture is expressed using an angle between the crystallographic direction parallel to the substrate normal and the $\langle 001 \rangle$ direction. The solid line marked “Fastest-growth Direction” in Fig. 12 is obtained by combining the α vs. $m_{N/Ti}$ reactor-scale results displayed in Fig. 7b with Equations 15 and 14 and by computing the angle between the $[hkl]$ direction defined by Equation 14 and the $\langle 001 \rangle$ direction. Also shown in Fig. 12 (denoted by arrow bars) are the ranges of grain orientations corresponding to the two coatings shown in Fig. 10a and b.

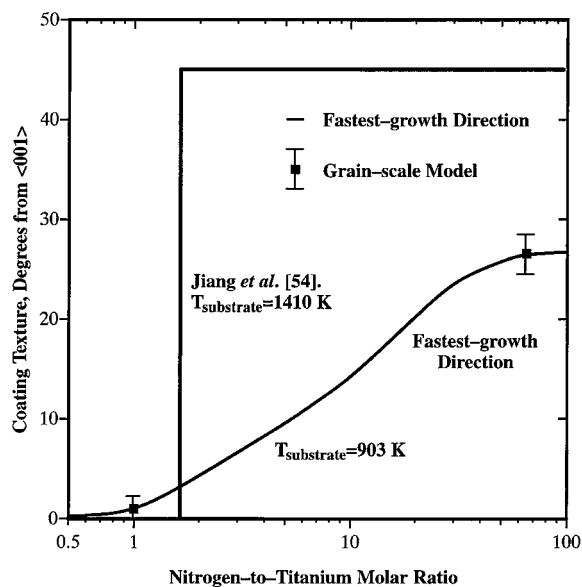


Figure 12 Variation of the crystallographic texture with the nitrogen-to-titanium molar ratio. Error bars indicate one standard deviation of the grain-scale modeling results over five runs.

Good agreement between the two sets of results suggests that the fastest-growth direction indeed governs the crystallographic texture in polycrystalline coatings. Also shown in Fig. 12 are the experimental results of Jiang *et al.* [54] at 1410 K which is the lowest temperature at which the transition between the $\langle 001 \rangle$ and the $\langle 011 \rangle$ texture is observed as $m_{N/Ti}$ is increased [54]. Since Jiang *et al.* [54] did not study the gradual evolution of the crystalline texture with process parameters, but rather tried to identify ranges of the process parameters in which one type of texture is dominant, their results can be represented only using a step function. The present model correctly predicts that as $m_{N/Ti}$ increases at 903 K, the texture is gradually evolving from the $\langle 001 \rangle$ type toward the $\langle 011 \rangle$ type. Furthermore, in good agreement with the results of Jiang *et al.* [54], the model predicts that at 903 K, the $\langle 011 \rangle$ -type texture does not fully develop.

As discussed earlier, the growth of polycrystalline TiN coatings takes place by the growth of $\{100\}$ and $\{111\}$ facets in the direction normal to themselves. Atomic-scale simulation results displayed in Fig. 8a and b show that $\{100\}$ - and $\{111\}$ -oriented TiN facets have different tendencies toward incorporating various crystal defects during the deposition process. Therefore in judging the potential quality of CVD-grown polycrystalline TiN coatings, it is important to consider what fraction of the coating volume is grown from the $\{100\}$ and what fraction from the $\{111\}$ facets. These fractions can be determined by plotting the trace of all the vertices associated with each grain in Fig. 10a and b. These traces partition each grain in up to three regions, where each facet is grown from a different surface facet.

The fraction of the coating volume grown from the $\{100\}$ facets, f_{100} , as a function of the coating thickness for the two selected values of the growth-rate parameter α is shown in Fig. 13. The results shown in Fig. 13 indicate that for $\alpha = 2.01$, the fraction of the coating volume grown from the $\{100\}$ facets does not change significantly and that it remains in the range 0.4–0.5. In

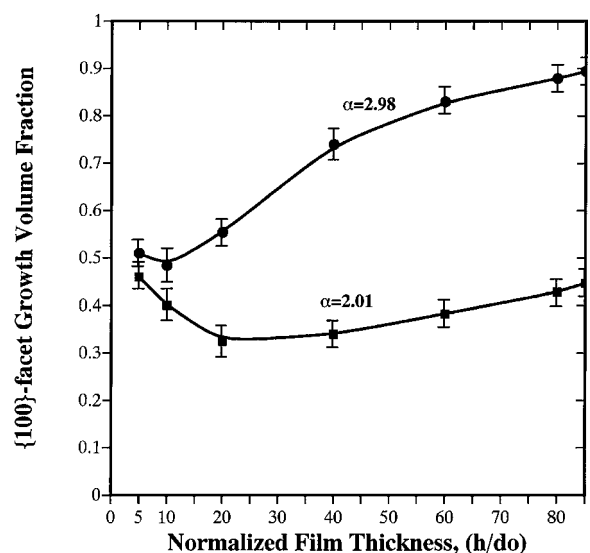


Figure 13 Variation of volume fraction of the coating grown from the $\{100\}$ -facets with the film thickness for two values of the growth rate parameter, α . Error bars indicate one standard deviation over five runs.

sharp contrast, for $\alpha = 2.98$, f_{100} changes substantially with the coating thickness so that the coating growth becomes dominated by the {100} facet-growth at the later stages of deposition. These findings are fully consistent with the corresponding growth-governing nuclei, Table V and the corresponding microstructure evolution results, Fig. 10a and b. In the original nuclei, the {100} and the {111} facets are present with statistically equal probabilities and hence $f_{100} \approx 0.5$. In the $\alpha = 2.01$ case, the film is dominated by the grains originating from the nuclei of types 2D3a, 2D3b and 2D4a. The top surface of such grains is bounded by the {100}, the {111} and the {111}/ $\overline{\{111\}}$ facets and hence in this case f_{100} should remain near 0.5 as the coating thickens.

For $\alpha = 2.98$, the coating growth is dominated by grains derived from the 2D4a nuclei. In these grains, the film growth is initially dominated by the {111} facets and thus f_{100} decreases below 0.5. However, at large coating thicknesses, the growth of the {111} facets is hampered in the lateral direction and, as evidenced by the coating microstructure displayed in Fig. 10a, and the coating surface becomes dominated by the {100} facets. As a result, f_{100} starts to increase with film thickness.

6. Discussion and conclusions

The work presented in this paper shows that by applying the methods for modeling the CVD of TiN coatings one can establish the relationship between the process parameters (e.g. chemistry of the feed gas, substrate temperature and reactor pressure), the coating deposition rate, the microstructure of the coating (including microstructural and crystallographic textures), its surface morphology and roughness and its quality (measured by an inverse of the concentration of various defects). Once these relations are established, they can be used to either optimize the CVD process (process optimization), to maximize the performance of the coating (product optimization), or both. In each of such optimization procedures, one must define the appropriate objective function which must be maximized. For instance, the ratio of the coating growth rate and the defect concentration represents one of such function for the product optimization, since its maximization ensures a high-production-rate low-defect coating. By combining the deposition-rate results, Fig. 7a, with the defect concentration data, Fig. 8a and b, $m_{N/Ti} = 6-8$ is identified as the optimal range of the nitrogen-to-titanium molar ratio at 903 K and at a condition NH_3 concentration in the feed gas of 1.94%.

It should be pointed out that further improvements in the present multi-length scale modeling scheme are needed before it can be used as a process/product optimization tool. Primarily, a more realistic model for surface diffusion has to be developed in order to improve agreement between the deposition rates predicted by the reactor-scale and atomic-scale methods. While the current modeling scheme predicts a correct trend in the effect of nitrogen-to-titanium ratio on the deposition rate, Fig. 7a, better agreement between the reactor-scale and the atomic-scale modeling predictions is needed to achieve the mutual consistence of the two approaches.

Such consistency is critical since both approaches are based on the same set of surface reactions and utilize the same reaction rate parameters. Furthermore, such consistence must be achieved while maintaining good agreement with the experimental data. In our previous work on multi-length scale modeling of the CVD of diamond films [31], where surface diffusion plays a considerably less important role, and hence was neglected, the predictions made by the reactor-scale and the atomic-scale method are found to be mutually fully consistent over a wide range of deposition parameters. Since the required rates of surface reactions accompanying the CVD of TiN are available only at 903 K, the entire analysis presented in this paper is carried out only at this temperature. However, the analysis can be readily extended to other temperatures once the relevant reaction rate data become available. Also, the approach is not limited to the TiN coatings and can be extended to other materials systems.

Finally, few basic conclusions can be drawn based on the analysis and the results presented in the paper:

(1) To establish the relationships between the process parameters, deposition condition and the microstructure (and thus properties) of CVD-grown coatings entails the use of a multi-length scale analysis which encompasses the reactor, atomic and grain length scales.

(2) The process parameters (e.g. feed-gas chemistry, reactor pressure, etc.) enter the analysis through a reactor-scale model which yields the deposition conditions. Such as the coating deposition rate and concentration of the various species on the coating surface.

(3) The morphology and the growth rate of surface facets and the mechanisms and the rates of incorporation of various crystal defects in the coating are determined through the use of an atomic-scale modeling scheme. Since the reactor scale and the atomic scale models use the same set of surface reactions, their predictions regarding the deposition rate must be mutually consistent. In the present formulations, the predictions of the two models for the deposition rates of TiN coatings are nearly consistent.

(4) The surface morphology and roughness, microstructure, the crystallographic texture as well as the defect content in the CVD-grown coatings are obtained using a grain-scale modeling scheme. While a two-dimensional grain-scale model is used in the present model, the crystallographic nature of the nuclei is selected in such a way that a direct comparison is possible between the model predictions and (three-dimensional) microstructure and crystallographic texture of coatings.

Acknowledgements

The work presented here has been supported by the U.S. Army Research Office, Grant DAAH04-96-1-0197 and Grant DAAD19-99-1-0096. The authors are indebted to Dr. David M. Stepp of ARO for the continuing interest in the present work. Encouragement and friendship of Professors R. J. Diefendorf and R. Singh is greatly appreciated. The authors also acknowledge the support of the Office of High Performance Computing Facilities at Clemson University.

References

1. R. S. BONETTI and O. F. HAPPEL, "Protective Coatings by Chemical Vapor Deposition in an Industrial Scale," BERNAG AG Olten, BERNEX Division, CH-4600 Olten, Switzerland, <http://www.multi-arc.com/coatings/technicalpapers/45.pdf>
2. J. E. SUNDGREN, *Thin Solid Films* **128** (1985) 21.
3. K. H. HABIG, *J. Vac. Sci. Technol.* **A4** (1986) 2832.
4. P. J. BURNETT and D. S. RICHERBY, *J. Mater. Sci.* **23** (1988) 2429.
5. W. D. SPROUL, *J. Vac. Sci. Technol.* **A4** (1986) 2874.
6. J. S. CHO, S. W. NAM and J. S. CHUN, *J. Mater. Sci.* **17** (1982) 2495.
7. M. S. KIM and J. S. CHUN, *Thin Solid Films* **107** (1983) 129.
8. C. H. J. VAN DEN BREKEL, R. M. M. FONVILLE, P. J. M. VAN DER STRATEN and G. VERSPUI, in "Proceedings of the 8th International Conference on Chemical Vapour Deposition," edited by J. M. Blocher, J. Wahl and G. E. Vuillard (Electrochemical Society, Princeton, NJ, 1981) p. 142.
9. F. TEYSSANDIER, C. BERNARD and M. DUCARROIR, in "Proceedings of the 6th European Conference on Chemical Vapor Deposition," edited by R. Porat (Iscar, Jerusalem, 1987) p. 96.
10. N. J. ARCHER, "Chemical Vapour Deposition," <http://www.multi-arc.com/coatings/technicalpapers/49.pdf>
11. R. S. LARSON and M. D. ALLENDORF, in "Proceedings of the 13th International Symposium on Chemical Vapor Deposition, Los Angeles, Vol. 96-5 (1996) p. 41.
12. Y. L. YANG and M. P. D'EVENLYN, *J. Amer. Chem. Soc.* **114** (1992) 2796.
13. T. FRAUENHWIM, U. STEPHAN, P. BLAUDECK, D. POREZAG, H.-G. BUSMANN, W. ZIMMERMANN-EDLING and S. LAUER, *Phys. Rev.* **B48** (1993) 18189.
14. Z. JING and J. L. WHITTEN, *Surf. Sci.* **314** (1994) 300.
15. S. SKOKOV, C. S. CARMER, B. WEINER and M. FRENKLACH, *Phys. Rev.* **B49** (1994) 5662.
16. S. CIRACI and I. P. BATRA, *ibid.* **B15** (1977) 3254.
17. S. F. YANG, D. A. DRABOLD and J. B. ADAMS, *ibid.* **B48** (1993) 5261.
18. B. N. DAVIDSON and W. E. PICKETT, *ibid.* **B49** (1994) 11253.
19. D. W. BRENNER, *ibid.* **B42** (1990) 9458.
20. B. J. GARRISON, E. J. DAWNKASKI, D. SRIVASTAVA and D. W. BRENNER, *Science* **255** (1992) 835.
21. D. HUANG and M. FRENKLACH, *J. Phys. Chem.* **96** (1992) 1868.
22. V. I. GAVRILENKO, *Phys. Rev.* **B47** (1993) 9556.
23. M. M. CLARK, L. M. RAFF and H. L. SCOTT, *Comput. Phys.* **10** (1996) 584.
24. C. C. BATTAILE, D. J. SROLOVITZ and J. E. BUTLER, *J. Appl. Phys.* **82** (1997) 6293.
25. M. GRUJICIC and S. G. LAI, *J. Mater. Sci.* **34** (1999) 7.
26. D. J. PARITOSH, C. C. SROLOVITZ, X. LI. BATTAILE and J. E. BUTLER, *Acta Mater.* **47** (1999) 2369.
27. M. GRUJICIC and S. G. LAI, *J. Mater. Sci.*, submitted.
28. *Idem.*, *ibid.* submitted.
29. J. S. CUSTER and P. M. SMITH, unpublished data.
30. SURFACE CHEMFIN III User Manual, Sandia National Laboratories, San Diego, CA 1996.
31. M. GRUJICIC and S. G. LAI, *J. Mater. Sci.* submitted.
32. G. EVANS and R. GREIF, *J. Heat Trans. ASME* **109** (1987) 928.
33. G. EVANS and R. GREIF, *Num. Heat Transfer* **12** (1987) 243.
34. M. E. COLTRIN, R. J. KEE and G. H. EVANS, *J. Electrochem. Soc.* **136** (1989) 819.
35. M. GRUJICIC and X. W. ZHOU, *Calphad* **17** (1993) 383.
36. M. GRUJICIC and P. DANG, *Mater. Sci. Eng.* **A205** (1996) 139.
37. R. A. ANDRIEVSKI, *J. Mater. Sci.* **32** (1997) 4463.
38. A. F. VOTER, *Phys. Rev. B* **34** (1986) 6819.
44. C. WILD, P. KOIDL, W. MÜLLER-SEBERT, H. WALCHER, R. KOHL, N. HERRES and R. LOCHER, *Diamond and Related Materials* **2** (1993) 158.
45. C. C. BATTAILE, D. J. SROLOVITZ and J. E. BUTLER, *J. Elec. Mater.* **26** (1997) 960.
46. A. VAN DER DRIFT, *Philips Res. Rep.* **22** (1967) 267.
47. C. WILD, N. HERRES and P. KOIDL, *J. Appl. Phys.* **68** (1990) 973.
48. C. J. CHU, R. H. HAUGE, J. L. MARGRAVE and M. P. D'EVELYN, *Appl. Phys. Lett.* **61** (1992) 1393.
49. R. A. ROY and R. MESSIER, *High Performance Ceramic Films and Coatings*, edited by P. Vincenzini (Elsevier Science Publishers B. V., Amsterdam, 1991) p. 367.
50. A. N. KOLMOGOROV, *Dokl. Akad. Nauk SSSR* **65** (1949) 681.
51. A. J. DAMMERS and S. RADELAAR, in Proceedings of the CP90 Europhysics Conference on Computational Physics, edited by A. Tenner (World Scientific, Singapore, 1991) p. 310.
52. J. M. THIJSSSEN, H. J. KNOPS and A. J. DAMMERS, *Phys. Rev. B* **45** (1992) 8650.
53. Y. VON KAENEL, J. STIEGLER, E. BALNK, O. CHAUVET, C. HELLWIG and K. PLAMANN, *Physica Status Solidi (a)* **154** (1996) 219.
54. C. JIANG, T. GOTO and T. HIRAI, *J. Mater. Sci.* **29** (1994) 669.

Received 24 April
and accepted 20 December 2000